AIAA JOURNAL
Vol. 36, No. 7, July 1998

Flow Through a Curved Duct Using Nonlinear Two-Equation Turbulence Models

Fotis Sotiropoulos* and Yiannis Ventikos†
Georgia Institute of Technology, Atlanta, Georgia 30332-0355

Standard isotropic and nonlinear two-equation turbulence closures are employed to calculate the flow through a 90-deg rectangular duct. The models used include the two-layer k-ε model, the k-ω model, and two nonlinear variants of the k-ω model based on quadratic and cubic constitutive relations, respectively. Comparisons of the computed results with the measurements show that the cubic nonlinear k-ω closure is the only model that successfully reproduces most of the experimentally observed features of both the mean flow and turbulence fields. This work demonstrates, for the first time, that near-wall, nonisotropic, two-equation models offer a promising alternative to Reynolds-stress transport closures for developing practical computational fluid dynamics methods able to predict complex shear flows of engineering interest.

Introduction

RECENT work in the area of advanced turbulence modeling has demonstrated the potential of Reynolds-stress transport (RST) models in predictions of complex, three-dimensional shear flows. A series of successful applications of such models to both internal[1,2] and external[3] flows has clearly underscored the need for adopting advanced turbulence modeling strategies to develop predictive computational fluid dynamics (CFD) methods for flows of engineering interest. Despite their success, RST models are not practical for simulating real-life flows because they require the solution of seven additional transport equations. With the rapid development of efficient numerical methods (see, for example, Ref. 4) and faster supercomputers, this requirement may not be too restrictive for steady-state simulations. It could, however, prove to be prohibitively expensive in predictions of unsteady three-dimensional flows. Nonlinear, two-equation turbulence closures offer a more realistic alternative in that regard, as they can, at least in principle, account for turbulence anisotropy effects at a substantially lower computational overhead. Such models may be constructed by combining a standard two-equation eddy-viscosity model with explicit, nonlinear constitutive equations that express the components of the Reynolds-stress tensor in terms of the mean rate-of-strain and rotation tensors. Several such constitutive relations have been recently proposed in the literature[5–7] and have been shown to yield encouraging results for two-dimensional shear flows. Their performance, however, in complex, three-dimensional flows, which exhibit most features encountered in real-life flow cases, has yet to be evaluated.

This paper seeks to explore the predictive capabilities of nonlinear eddy-viscosity models—relative to each other and to standard isotropic models—by applying them to calculate the flow through a 90-deg rectangular duct for which detailed experimental measurements are available.[8] In the following sections, we review the recent developments in the area of advanced turbulence modeling for three-dimensional flows. Subsequently, we outline the objectives of the present contribution and give a brief overview of this paper.

Previous Work and the Present Contribution

Sotiropoulos and Patel[1–3] were the first to report successful applications of a full near-wall RST closure to internal and external, three-dimensional flows. They employed the Launder and Shima[9] (LSH) model (with the modifications proposed by Shima[10]) to calculate the flow through a circular-to-rectangular transition duct for which detailed measurements were reported by Davis and Gessner.[11] Previous attempts to resolve this flow using two-layer and low-Reynolds-number isotropic k-ε models[12,13] were not successful, as they grossly underestimated the strength of the longitudinal vortices developing within the transition region. The RST closure employed by Sotiropoulos and Patel,[1] on the other hand, was successful in reproducing, for the first time, most of the experimentally observed features within the transition region. In particular, the origin and growth of longitudinal vorticity and its interaction with the mean streamwise flow and Reynolds stresses were resolved with remarkable accuracy. Some discrepancies were observed at the end of the straight section downstream of the transition region where the predicted relaxation of the turbulence quantities towards equilibrium appeared to occur faster than that implied by the measurements.[1]

In a more recent study, Sotiropoulos and Patel[2] employed the same transition duct test case to demonstrate the role of turbulence anisotropy and near-wall modeling in predictions of complex, three-dimensional flows. They carried out calculations using the standard k-ε model and the RST model of Gibson and Launder,[14] both with wall functions. They compared these solutions with the earlier LSH predictions and measurements and concluded that accurate description of most three-dimensional turbulent flows, regardless of their origin, requires turbulence models that resolve the near-wall flow and account for anisotropy of the Reynolds stresses. Additional evidence to support such a conclusion was provided in yet another recent study by Sotiropoulos and Patel,[3] who calculated the flow past two ship hulls using a two-layer k-ε model and the LSH model. The LSH model reproduced most of the experimentally observed flow features, including the origin and growth of intense stern vortices and the resulting distortion of the mean streamwise velocity field, whereas the two-equation model was able to predict only the general trends of the data.

The objective of this paper is to investigate the potential of nonlinear (or nonisotropic), two-equation, eddy-viscosity models as more practical alternatives to RST closures in predictions of three-dimensional flows. Two isotropic eddy-viscosity models and two nonlinear models are investigated herein. The isotropic models include the two-layer k-ε model of Chen and Patel[15] and the k-ω model of Wilcox.[16] The nonlinear closures are those constructed by Abid et al.[17] and Sofialidis and Prinos,[18] who combined the linear k-ω model with the nonlinear constitutive equations by Gatski and Speziale[6] (GS) and Craft et al.[7] (CLS), respectively. In our subsequent discussion, these two models will be referred to as k-ω (GS) and k-ω (CLS). All turbulence models are implemented in an efficient finite volume algorithm for solving the Reynolds-averaged Navier–Stokes equations in generalized curvilinear coordinates. The method employs a multigrid artificial compressibility approach, and it is second order accurate in space.[4,19]

Received Feb. 26, 1997; revision received Feb. 15, 1998; accepted for publication March 12, 1998.

*Assistant Professor, School of Civil and Environmental Engineering. Member AIAA.
†Postdoctoral Associate, School of Civil and Environmental Engineering.

The experiment of Kim and Patel[8] (see also Ref. 20), who reported detailed mean flow and turbulence statistics measurements for flow through a 90-deg rectangular duct, is selected as a test case for evaluating the various turbulence models. This case was among the test cases that were studied numerically in the recent ERCOFTAC-IAHR Workshop on Refined Flow Modeling.[21] Participants to this workshop employed a large variety of turbulence closures, including the standard k-ε model with wall functions, near-wall linear and nonlinear two-equation models, as well as full RST models. However, the relatively coarse meshes employed by most contributors, the use of numerical methods of varying degree of spatial resolution, and differences in the inflow conditions did not facilitate meaningful evaluation of the computed results. It was commonly observed, for instance, that contributors who employed identical turbulence models got substantially different results. The present work seeks to carry out a systematic evaluation of the various turbulence models by carefully eliminating such uncertainties.

In what follows, we first present the governing equations of the various turbulence models, describe briefly the numerical method, and discuss various computational details. Subsequently, the computed results are compared with each other and with the measurements of Kim and Patel.[8] Comparisons include profiles of mean velocity components and contours of mean streamwise vorticity and turbulence statistics.

Turbulence Models

In this section, we summarize the constitutive relations of Gatski and Speziale[6] and Craft et al.,[7] which are combined with the k-ω transport equations to construct the two nonlinear models. Because of space considerations, the reader is referred to Ref. 16 and Ref. 15 for a detailed description of the isotropic k-ω and two-layer k-ε models, respectively. Here it suffices to emphasize that the constants in both models are identical to those given in their respective references. For the k-ω model, we should also point out that wall boundary conditions for ω are specified following Menter.[22]

Speziale and Gatski Constitutive Relation

The explicit, quadratic constitutive equation of Gatski and Speziale[6] is given as follows:

$$\overline{u_i u_j} = \tfrac{2}{3}k\delta_{ij} - 2v_t\left[\tfrac{1}{2}S_{ij} + \alpha_4(1/4\omega)(S_{ik}\Omega_{kj} - S_{jk}\Omega_{ki}) - \alpha_5(1/4\omega)(S_{ik}S_{kj} - S_{jk}S_{ki})\right] \tag{1}$$

where $S_{ij} = U_{i,j} + U_{j,i}$ and $\Omega_{ij} = U_{i,j} - U_{j,i}$. The definition of the eddy viscosity v_t, the expressions for the various constants in Eq. (1), as well as the modeled k-ω transport equations employed in conjunction with Eq. (1), can be found in Ref. 17 (denoted as model A in that paper).

Craft et al. Constitutive Relation

Craft et al.[7] proposed a constitutive Reynolds-stress relation involving nonlinear terms up to cubic order, that reads as follows:

$$\begin{aligned}\overline{u_i u_j} = {} & \tfrac{2}{3}k\delta_{ij} - v_t\left\{S_{ij} - (k/\varepsilon)\left[c_1\left(S_{ik}S_{kj} - \tfrac{1}{3}S_{pq}S_{pq}\delta_{ij}\right)\right.\right. \\ & + c_2(\Omega_{ik}S_{kj} + \Omega_{jk}S_{ki}) + c_3\left(\Omega_{ik}\Omega_{kj} - \tfrac{1}{3}\Omega_{pq}\Omega_{pq}\delta_{ij}\right)\left.\right] \\ & - (k/\varepsilon)^2\left[c_4C_\mu\left(S_{ki}\Omega_{lj} + S_{kj}\Omega_{li} - \tfrac{2}{3}S_{km}\Omega_{lm}\delta_{ij}\right)S_{kl}\right. \\ & \left.\left. + c_6C_\mu S_{ij}S_{kl}S_{kl} + c_7C_\mu S_{ij}\Omega_{kl}\Omega_{kl}\right]\right\}\end{aligned} \tag{2}$$

The k-ω equations employed in conjunction with Eq. (2) and the definitions of the various coefficients can be found in Ref. 18.

Numerical Method

The numerical method of Lin and Sotiropoulos[4,19] is used in the present study. This method solves the three-dimensional Reynolds-averaged Navier–Stokes (RANS) equations, in conjunction with two-equation, near-wall turbulence closures, formulated in generalized curvilinear coordinates in strong conservation form. Pressure–velocity coupling is achieved using the artificial compressibility approach. The governing equations are discretized on a nonstaggered computational mesh using finite volume discretization schemes. Three-point central differencing is employed for the viscous fluxes and source terms in the turbulence closure equations. The convective terms are discretized using three-point, second-order accurate central differencing with explicitly added third-order matrix-valued artificial dissipation terms.[4,19] All solutions in this paper were obtained by setting the coefficient of the artificial dissipation terms equal to 0.004.

The discrete mean flow and turbulence closure equations are integrated in time using a four-stage explicit Runge–Kutta algorithm enhanced with local time stepping, implicit residual smoothing, and multigrid acceleration.[4] It should be noted that multigrid is applied herein only to the mean flow equations. A three-level V-cycle algorithm with semicoarsening in the transverse plane[4] is employed with one, two, and three iterations performed on the first, second, and third grid level, respectively. The turbulence closure equations are solved only on the finest mesh, and the eddy viscosity and Reynolds stresses are injected to the coarser meshes and held constant during the multigrid cycling process. Three single-grid iterations are performed on the turbulence closure equations per multigrid cycle.

Test Case and Computational Details

The experiment of Kim and Patel[8] and Kim[20] is selected as the test case for this study. They reported detailed mean flow and turbulence measurements for flow through a 90-deg rectangular duct, of aspect ratio 6, at Reynolds number $Re = 2.24 \times 10^5$ (based on the duct width and the mean bulk velocity). An overall view of the wind tunnel and duct geometry, as well as the locations of the measurement stations, is shown in Fig. 1. The flow enters the inlet tangent of the curved duct through a short transition duct (a two-dimensional 6:1 contraction). The transverse pressure gradients on the top wall of the contraction induce a pair of vortices inside the top-wall boundary layer resulting in a complex three-dimensional flow at the inlet of the upstream straight tangent.[20] To ensure that the inlet conditions for the numerical calculations properly represent the experimental situation, the experimental data at station U1 are used to construct appropriate inlet distributions for the mean velocity components and the turbulent quantities (see Ref. 20 for more details on using the measurements to construct inlet conditions for the calculations).

The computational domain starts $4.5H$ upstream from the inlet of the bend (station U1) and extends up to $30H$ downstream from

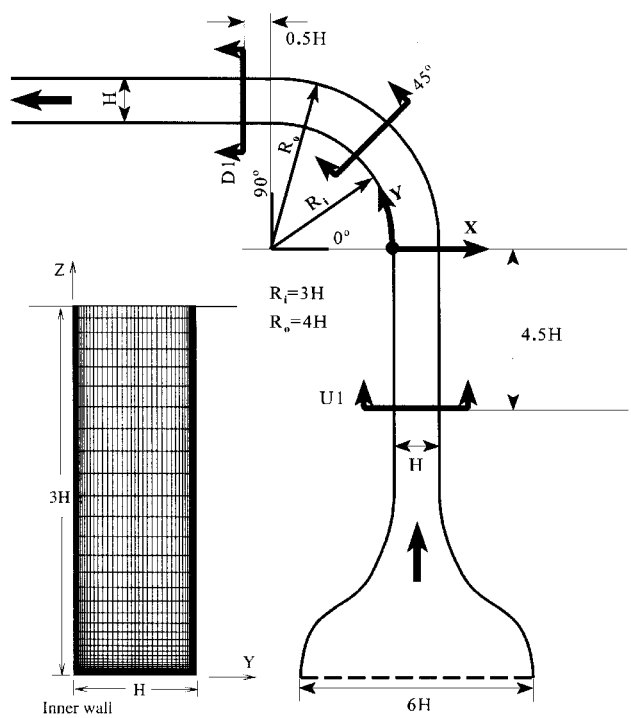

Fig. 1 Coordinates, measurement locations, and cross-sectional mesh for the curved duct of Kim and Patel.[8]

the exit of the bend. Because of symmetry, only half of the physical domain is modeled with symmetry conditions applied at $Z = 3$. A numerical mesh with $98 \times 69 \times 52$ nodes, in the streamwise, radial, and normal directions, respectively, is used for all subsequently reported calculations. The streamwise spacing inside the bend is 1.8 deg, whereas the first coordinate surface off the duct walls is located well within the laminar sublayer, around $y^+ = 0.75$, almost everywhere (the cross-sectional view of the mesh is shown in Fig. 1).

A partial grid sensitivity study was conducted by refining the mesh in the streamwise direction (a $150 \times 69 \times 52$ grid was employed). Calculations on this finer mesh were carried out using only the k-ω model. The computed results were in very good agreement with those obtained on the $98 \times 69 \times 52$ mesh. Thus, this coarser mesh was considered to be sufficiently fine for resolving the most important flow features. It should be noted, though, that no attempt was made to establish grid independent solutions. Given the number of turbulence closures studied herein and the overall dimensions of the geometry under consideration, such a study would require computer resources well beyond those at our disposal. This not withstanding, however, all turbulence models were applied on the same numerical mesh using the same numerical method. Thus, discrepancies between various calculations (see subsequent section) are due to the effect of the turbulence model rather than artifacts of varying levels of numerical diffusion. Furthermore, the accuracy of the matrix-valued artificial dissipation model employed herein has been thoroughly investigated by Lin and Sotiropoulos[4] and has been shown to drastically enhance numerical accuracy—as compared with other high-resolution discretization schemes—on high-aspect-ratio meshes.

For all turbulence models employed herein, convergence is declared after the residuals have been reduced by five orders of magnitude—a convergence level that is typically achieved after 2000–3000 multigrid cycles.

Results and Discussion

In this section we present comparisons between the calculations and the measurements of Kim and Patel[8] and discuss the physics of the flow along with the relative performance of the various models. Although mean velocity measurements are available at several streamwise stations (Fig. 1), due to space limitations only a sample of the computed results is compared with the data at two representative stations. The comparisons shown here include mean velocity profiles at stations 45 and D1 (Figs. 2 and 3) and mean streamwise vorticity (Figs. 4 and 5) and turbulence statistics contours (Figs. 6–10) at station D1.

At each streamwise station, mean velocity comparisons are shown at four $Z =$ const lines. One is always located at the plane of symmetry ($Z = 3.0$), whereas the others are selected separately, for each streamwise station, so that they span the region where three-dimensional effects are most prominent. The so-selected locations are $Z = 0.375, 0.625, 0.875$, and 3.0 for station 45 and $Z = 0.5, 0.75$, 1.0, and 3.0 for station D1. The three mean velocity components are expressed in terms of the coordinates shown in Fig. 1—that is, U, V, and W are along the streamwise, radial, and normal directions, respectively. The measured vorticity contours, shown in Figs. 4 and 5, were obtained by finite differencing the measured mean velocity field using second-order central differencing.

The measured streamwise vorticity and turbulence statistics contours shown in Figs. 4–10 exhibit small but clearly visible discontinuities across certain Y and $Z =$ const lines. The vorticity contours shown in Figs. 4 and 5 for instance, are discontinuous across the lines $Z = 1$ and $Y = 0.19$, respectively. Similar discontinuities are evident in all contour plots of the turbulence quantities (Figs. 6–10). Examination of the cross-sectional experimental mesh employed by Kim and Patel[8] reveals that it consists of several blocks of varying spatial resolution. The discontinuity lines observed in the measured contours coincide with the interfaces between the various blocks. Their cause is not known as Kim and Patel[8] do not discuss this point in their paper.

Finally, in all subsequent figures, the length and velocity scales used to nondimensionalize the various geometrical and flow quantities are H (Fig. 1) and U_o, respectively.

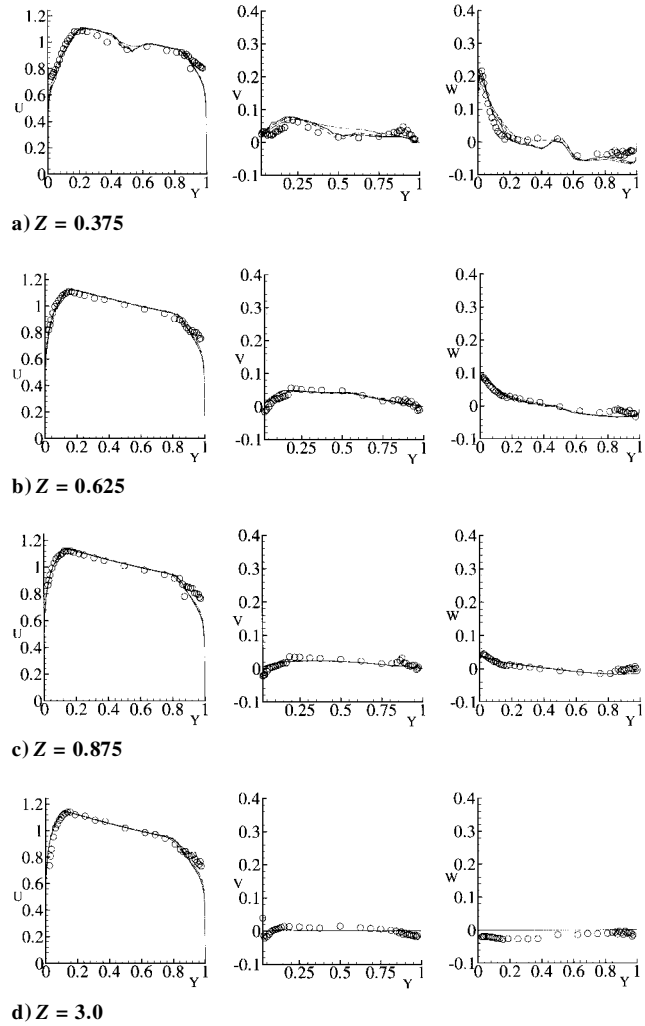

Fig. 2 Measured[8] and computed mean velocity profiles at station 45: ——, k-ω (CLS); - - -, k-ω (SG); —·—, k-ω; and —··—, k-ε.

Mean Velocity Profiles

Figure 2 shows measured and computed mean velocity profiles at station 45. The measured velocity profiles near the center of the bottom wall (Fig. 2a) are distorted, presumably due to the influence of the contraction-induced vortex pair that continues to affect the flow well within the bend. A detailed description of the evolution of this vortex pair in the upstream tangent and within the bend can be found in Ref. 8. The favorable longitudinal pressure gradient along the inner wall accelerates the flow and causes the maximum of the axial velocity profile to shift from the center toward the convex wall of the bend. The transverse pressure gradients, on the other hand, give rise to a significant secondary motion as suggested by the sharp peak of the W profiles near the inner bend. This pressure-driven secondary motion acts to reduce the mean streamwise velocity near the inner wall by transporting there low-momentum fluid from the bottom wall boundary layer (see the U-velocity profile at $Z = 0.375$). As seen in Fig. 2, the strength of the secondary motion, which is approximately 20% of the bulk velocity near the bottom wall, decays rapidly as the plane of symmetry is approached. All three k-ω based models yield almost identical results, which are in good agreement with the measurements. The k-ε predictions are also in close agreement with the measurements except near the bottom wall ($Z = 0.375$) where the predicted peak of the W component is underestimated. A rather noteworthy discrepancy between the data and all four predictions is observed near the outer wall of the bend where the thickness of the boundary layer is systematically overpredicted. This trend should be attributed to the apparent inability of both the linear and nonlinear closures to account for the destabilizing effects of concave curvature. A more detailed discussion of this issue is given in a subsequent section of this paper.

Immediately downstream of the end of curvature (station D1; Fig. 3), the measurements suggest that the secondary motion near the inner wall intensifies and spreads upward toward the plane of symmetry. The axial velocity profiles are distorted by the intense secondary motion and become S-shaped near the inner bend (Figs. 3a and 3b). Unlike station 45 where all closures yielded very similar results, significant differences are observed herein between the various calculations. The best overall predictions are those obtained by the k-ω (CLS) closure. This model yields more distorted than measured axial velocity profiles near the inner wall but is the only one that reproduces several important experimental trends at $Z = 0.5$ and 0.75. For instance, the computed U profiles are S-shaped and attain their respective local maxima and minima near the inner wall at Y locations that agree well with the measurements (Fig. 3a). The other three closures yield S-shaped profiles that are considerably more diffused in the Y direction, a trend that is clearly evident at $Z = 0.5$ (Fig. 3a). Furthermore, only the k-ω (CLS) model captures correctly the strength of the secondary motion near the inner wall. All other closures underestimate significantly the positive peak in the W profile at $Z = 0.75$, with the k-ε model yielding the worst overall results. A consistent discrepancy between computed and measured W profiles is observed for $Y > 0.2$, where all closures systematically predict a stronger negative W component (Figs. 3a and 3b). Also, the previously discussed overestimation of the concave wall boundary-layerthickness is still evident in all four predictions, albeit not as pronounced as in station 45. Finally, it is interesting to note that the four models yield very similar results as the symmetry plane is approached and the flow becomes more two dimensional.

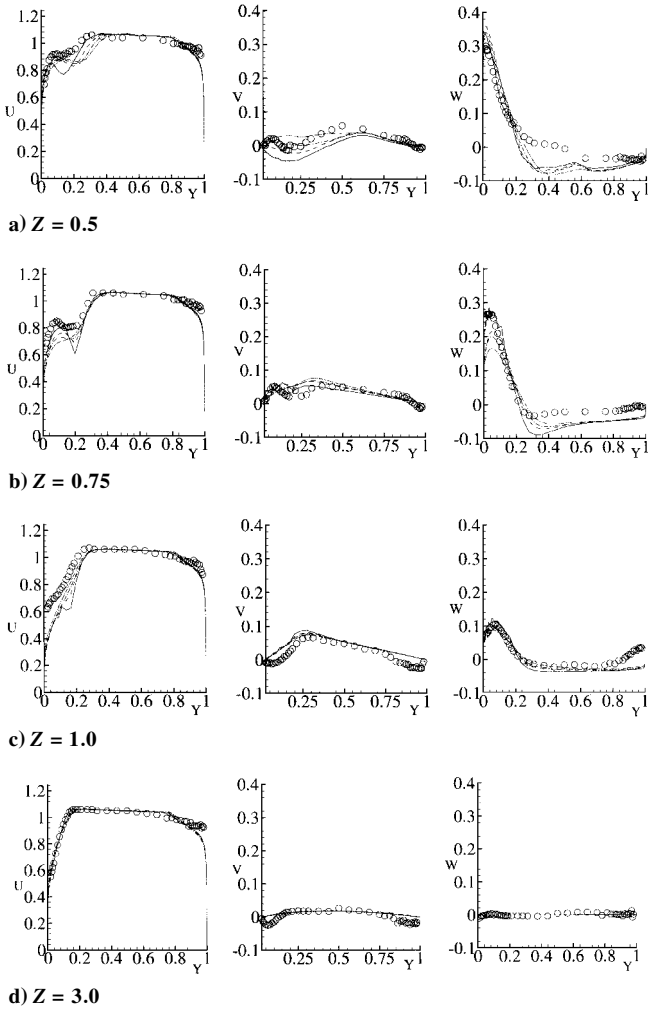

Fig. 3 Measured[8] and computed mean velocity profiles at station D1: ——, k-ω (CLS); - - -, k-ω (SG); —·—, k-ω; and —··—, k-ε.

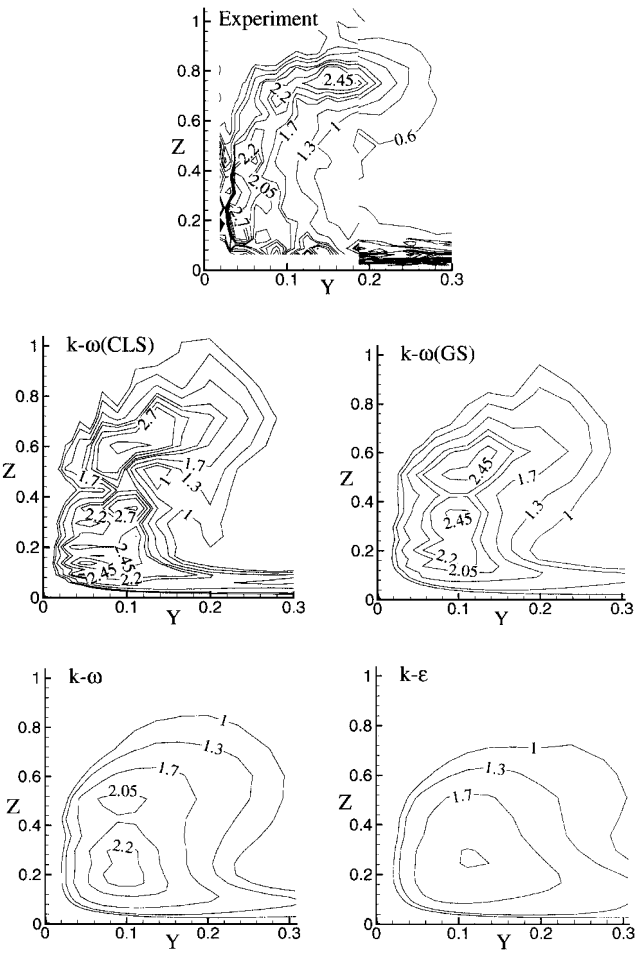

Fig. 5 Measured[8] and computed mean streamwise vorticity contours near the corner of the inner wall at station D1. Axis aspect ratio has been distorted for clarity.

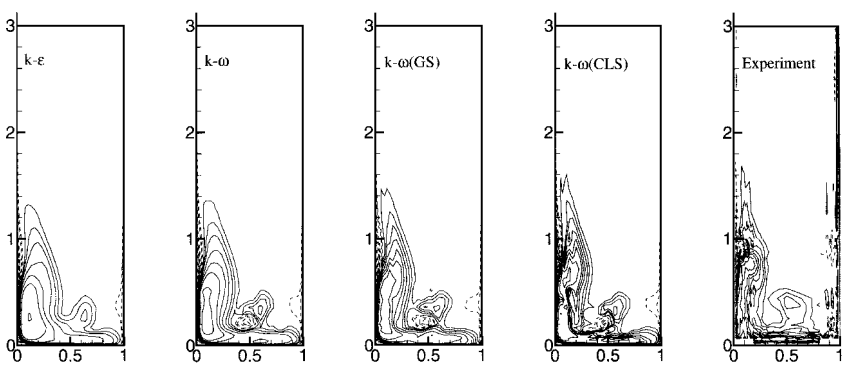

Fig. 4 Measured[8] and computed mean streamwise vorticity contours at station D1. Contour levels: ± 0.2, ± 0.4, ± 0.6, ± 0.9, ± 1.2, ± 1.5, ± 2.0, and ± 3.0.

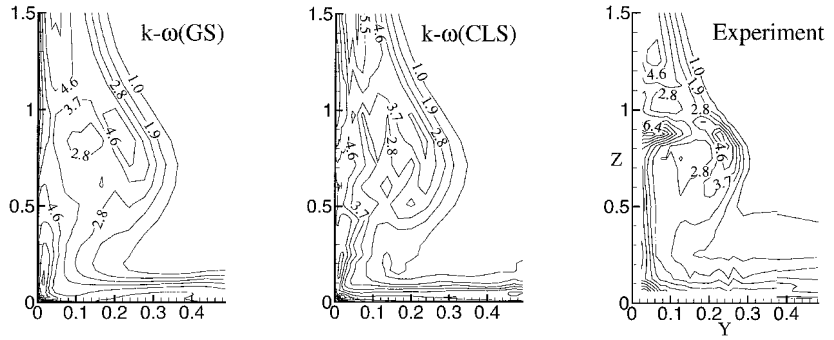

Fig. 6 Measured[8] and computed $10^3 \times \bar{u}^2$ contours near the corner of the inner wall at station D1. Axis aspect ratio has been distorted for clarity.

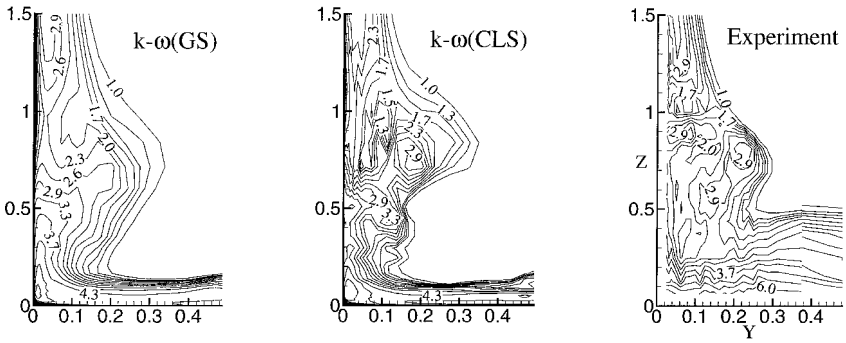

Fig. 7 Measured[8] and computed $10^3 \times \bar{v}^2$ contours near the corner of the inner wall at station D1. Axis aspect ratio has been distorted for clarity.

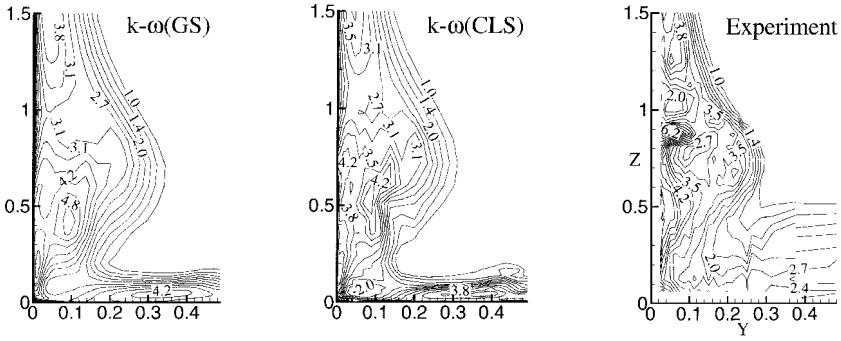

Fig. 8 Measured[8] and computed $10^3 \times \bar{w}^2$ contours near the corner of the inner wall at station D1. Axis aspect ratio has been distorted for clarity.

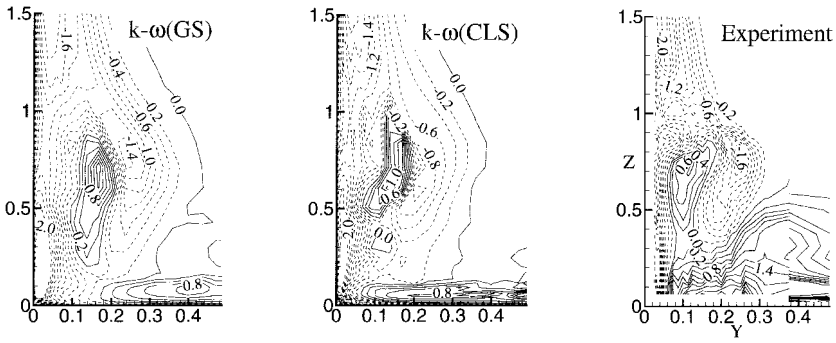

Fig. 9 Measured[8] and computed $10^3 \times \overline{uv}$ contours near the corner of the inner wall at station D1. Axis aspect ratio has been distorted for clarity.

Longitudinal Vorticity Field

The differences between the various predictions are even more pronounced in Fig. 4, which depicts measured and computed contours of constant streamwise vorticity at station D1. It is seen that along the bottom wall all three k-ω predictions yield two well-defined cores of positive and negative vorticity. Vorticity contours at previous stations within the bend, not shown herein due to space limitations, suggest that these vortices have evolved from the contraction-induced vortex pair. Recall that in all calculations this vortex pair was specified using the measurements at station U1. As seen in Fig. 4, the k-ω based models predict a region of intense vorticity gradients in the vicinity of the vortex pair. This suggests a rather complex interaction between the cores of positive and negative vorticity and the pressure-driven positive vorticity layer that develops along the bottom and inner wall junction. In fact, the positive vortex core appears to extract vorticity from this layer and curve around the negative core—these features are particularly pronounced in the k-ω (CLS) prediction. The measurements exhibit similar qualitative trends, but the spatial vorticity gradients are rather weak, and the negative vorticity region has almost disappeared. It should be noted, however, that comparisons between measured and computed vorticity contours cannot be entirely conclusive in this region due to the apparent lack of adequate spatial resolution in the experiment. More specifically, in all three k-ω predictions, the

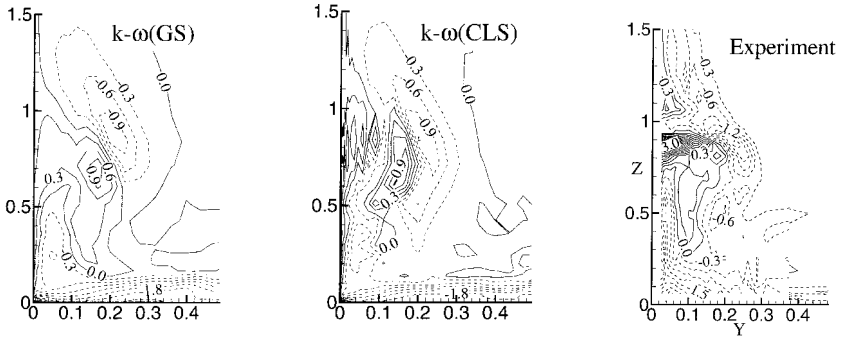

Fig. 10 Measured[8] and computed $10^3 \times \overline{uw}$ contours near the corner of the inner wall at station D1. Axis aspect ratio has been distorted for clarity.

width of the calculated positive vortex core is approximately equal to $0.13H$. Inspection of the experimental mesh employed by Kim and Patel[8] in this region reveals that the ΔY grid spacing is also of the same order. That is, even if the vortical structures implied by the k-ω predictions were indeed present in the flow, a significantly finer experimental mesh would be required to properly resolve them.

Along the inner bend, where measurements were obtained on a very fine mesh, the experiment reveals the presence of an elongated pressure-driven pocket of positive vorticity that spreads toward the plane of symmetry. The agreement between the measurements and the computations improves steadily from the k-ε to the k-ω (CLS) model. Consistent with the rather poor predictions of the three mean velocity components, the k-ε model yields very diffused vorticity contours. The k-ω predictions begin to exhibit some of the measured features, such as the spreading of the vorticity contours along the inner wall, but the overall structure of the vorticity field is considerably simpler than measured. Improved predictions, as compared with the two isotropic models, are obtained using the k-ω (GS) closure. The computed vorticity contours begin to exhibit the characteristic spiky structure seen in the measurements and become more elongated along the Z direction. These trends become significantly more pronounced in the k-ω (CLS) prediction, which captures most experimental features with remarkable accuracy, considering the complexity of the flow. More specifically, the computed vertical spread of the pocket of positive vorticity, its slender structure, and the complex shapes of the contours within $0.4 < Z < 1.0$ are now in good overall agreement with the measurements.

The preceding comparisons provide a general assessment of the performance of the various closures and clearly underscore the superiority of the k-ω (CLS) nonlinear model. Further evidence to support this conclusion is provided in Fig. 5, which shows an enlarged view of measured and predicted longitudinal vorticity contours at station D1 near the junction of the inner and bottom walls. This figure is the lower left corner detail of Fig. 4 with the axis aspect ratio distorted appropriately to clarify the structure of the vortex core. The measurements reveal a very complex vortex structure characterized by the presence of several distinct local vorticity maxima and C-shaped contours. The k-ω (CLS) closure is the only one that reproduces, even at this extremely magnified spatial scale, most of the experimental trends reasonably well. The computed contours are also C-shaped, although more diffused in the Y direction, and clearly exhibit several distinct peaks. All other closures fail to capture even general qualitative features of the measurements. The predicted vorticity contours are rather diffused, and the vortex core is located farther away from the inner wall of the bend.

Turbulence Statistics at Station D1

Measured and computed contours of turbulence statistics—$\overline{u}^2$, $\overline{v}^2$, $\overline{w}^2$, $\overline{uv}$, and $\overline{uw}$ (no $\overline{vw}$ measurements were reported by Kim and Patel[8])—at the lower left corner of station D1 are compared in Figs. 6–10. The objective of these comparisons is to evaluate the ability of the CLS and GS nonlinear models to capture the structure of the turbulence field in a very complex, three-dimensional flow. The two linear closures are not included herein, as it is evident from our previous discussion that they fail to capture even the most essential features of the mean flow. For the sake of clarity, the axis aspect ratio in Figs. 6–10 has been distorted appropriately

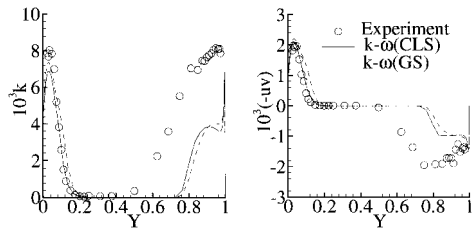

Fig. 11 Measured[8] and computed $10^3 \times k$ and $10^3 \times \overline{uv}$ plane-of-symmetry profiles at station D1.

to elucidate the structure of the various turbulence quantities in the vicinity of the complex longitudinal vortex core.

The general features of the measured turbulence statistics contours are consistent with those associated with the interaction of a longitudinal vortex with a boundary layer. The distortion of the mean flow in the vicinity of the vortex (Fig. 3) results in increased turbulence production by mean shear, which is responsible for the formation of the observed pocket (Figs. 6–10) of increased Reynolds stresses along the inner wall. Within this pocket, $\overline{uv}$ and $\overline{uw}$ change sign as a result of the intense transport of momentum and energy by the vortex. Both models reproduce the general shapes of the measured contours reasonably well. The most notable discrepancies between the two closures are observed in the predictions of the $\overline{v}^2$ contours. As seen in Fig. 7, the k-ω (GS) fails to predict the two distinct, nearly circular, pockets of increased $\overline{v}^2$, which are successfully reproduced by the k-ω (CLS) model. Similar disagreements between the k-ω (GS) closure and the measurements are also observed in the $\overline{uw}$ contours shown in Fig. 8. The measurements reveal a rather intense pocket of negative $\overline{uw}$ wrapping around the region of positive $\overline{uw}$. Only the k-ω (CLS) model captures this feature reasonably well, although some discrepancies are observed in the internal structure of the pocket of positive $\overline{uw}$. An important systematic disagreement between measurements and calculations is seen along the bottom wall where both closures underpredict the thickness of the layer of increased turbulence intensities (Figs. 6–10). This not withstanding, however, the results of this study are particularly encouraging. The preceding comparisons demonstrate that a relatively simple, compared with a full Reynolds-stress transport model, two-equation closure is capable of resolving not only the mean flow but also the general structure of the turbulence statistics in a very complex, highly three-dimensional shear flow.

Finally, Fig. 11 shows comparisons of turbulence kinetic energy and $\overline{uv}$ profiles at the plane of symmetry at station D1. Both closures perform well near the inner (convex) wall but fail to capture the spectacular increase of turbulence kinetic energy and shear stress near the concave wall. These discrepancies are consistent with the previously discussed overestimation of the boundary-layer thickness near the outer wall. They are in agreement with the well-known inability of two-equation models to account for the destabilizing effects of concave curvature, at least not without explicitly added curvature corrections.[23] The present results further demonstrate similar inadequacies for nonlinear two-equations models as well. These comparisons point to the need for further modeling refinements to properly account for concave curvature effects. A recent study by Luo and Lakshminarayana,[24] who carried out two-dimensional

(plane-of-symmetry) calculations for several curved ducts using RST models, appears to suggest that such refinements should focus on sensitizing the turbulence length-scale equation to concave curvature effects.

Summary and Conclusions

Standard isotropic and nonlinear two-equation eddy-viscosity models were implemented in a finite volume multigrid method and applied to calculate flow though a rectangular 90-deg bend. The computed solutions were compared with available mean flow and turbulence statistics measurements. The following conclusions are drawn from the present study.

The isotropic two-layer k-ε and k-ω models are inadequate for resolving complex three-dimensional flows. Although the k-ω model gives relatively better results, both closures underpredict the strength of the pressure-driven secondary motion and produce a weak, highly diffused streamwise vorticity field. The quadratic nonlinear k-ω (GS) model improves somewhat the prediction of the mean flow but yields a vorticity field at the exit of the bend that is considerably more diffused and of simpler structure than measured.

Significantly improved predictions are obtained using the cubic k-ω (CLS) model, which, in agreement with the measurements, produces a very complex vortex core characterized by multiple vorticity peaks. The k-ω (CLS) model also yields the best overall predictions for the Reynolds stresses in the region where the pressure-driven longitudinal vortex interacts with the inner wall boundary layer. These results, along with the failure of the two isotropic models, provide additional evidence to support earlier conclusions that accurate predictions of most three-dimensional flows necessitate the use of near-wall, nonisotropic turbulence models.

None of the turbulence closures employed herein were successful in resolving the measured spectacular increase of turbulence kinetic energy and shear stress near the concave wall of the bend. Although the inability of standard two-equation models to predict the effects of concave curvature is well known, the present work demonstrates similar inadequacies with nonlinear models.

Although important discrepancies between the k-ω (CLS) predictions and the measurements still remain, the results of this study are very encouraging. They demonstrate, for the first time, that nonlinear two equation models, which are computationally more efficient than Reynolds-stress transport models, can provide a practical framework for developing predictive CFD methods for flows of industrial interest.

Acknowledgments

This research was supported by a grant from Voith Hydro, Inc., monitored by R. K. Fisher Jr. under the Department of Energy's Advanced Hydroturbine Project. The calculations were carried out on the Cray C90 machine of the San Diego Supercomputer Center. The authors are grateful to V. C. Patel and W. J. Kim for providing the experimental measurements and the subroutine for generating the inlet conditions.

References

[1] Sotiropoulos, F., and Patel, V. C., "Prediction of Turbulent Flow Through a Transition Duct Using a Second-Moment Closure," *AIAA Journal*, Vol. 32, No. 11, 1994, pp. 2194–2204.

[2] Sotiropoulos, F., and Patel, V. C., "On the Role of Turbulence Anisotropy and Near-Wall Modeling in Predicting Complex, 3D, Shear Flows," *AIAA Journal*, Vol. 33, No. 3, 1995, pp. 504–514.

[3] Sotiropoulos, F., and Patel, V. C., "Application of Reynolds-Stress Transport Models to Stern and Wake Flows," *Journal of Ship Research*, Vol. 39, No. 4, 1995, pp. 263–283.

[4] Lin, F., and Sotiropoulos, F., "Strongly-Coupled Multigrid Method for 3-D Incompressible Flows Using Near-Wall Turbulence Closures," *Journal of Fluids Engineering*, Vol. 119, No. 2, 1997, pp. 314–324.

[5] Shih, T. H., Zhu, J., and Lumley, J. L., "A New Reynolds-Stress Algebraic Equation Model," *Computational Methods in Applied Mechanics*, Vol. 125, 1995, pp. 287–302.

[6] Gatski, T. B., and Speziale, C. G., "On Explicit Algebraic Stress Models for Complex Turbulent Flows," *Journal of Fluid Mechanics*, Vol. 254, 1993, pp. 59–78.

[7] Craft, T. J., Launder, B. E., and Suga, K., "A Non-Linear Eddy-Viscosity Model Including Sensitivity to Stress Anisotropy," *Proceedings of 10th Symposium on Turbulent Shear Flows*, Pennsylvania State Univ., State College, PA, 1995.

[8] Kim, W. J., and Patel, V. C., "Origin and Decay of Longitudinal Vortices Developing in a Curved Rectangular Duct," *Journal of Fluids Engineering*, Vol. 116, No. 1, 1994, p. 45.

[9] Launder, B. E., and Shima, N., "Second-Moment Closure for the Near-Wall Sublayer: Development and Application," *AIAA Journal*, Vol. 27, No. 10, 1989, pp. 1319–1325.

[10] Shima, N., "Prediction of Turbulent Boundary Layers with a Second-Moment Closure: Part I—Effects of Periodic Pressure Gradient, Wall Transpiration, and Free-Stream Turbulence," *Journal of Fluids Engineering*, Vol. 115, No. 1, 1993, pp. 56–63.

[11] Davis, D. O., and Gessner, F. B., "Experimental Investigation of Turbulent Flow Through a Circular-to-Rectangular Transition Duct," *AIAA Journal*, Vol. 30, No. 2, 1992, pp. 367–375.

[12] Sotiropoulos, F., and Patel, V. C., "Flow in Curved Ducts of Varying Cross-Section," Iowa Inst. of Hydraulics Research, IIHR Rept. 358, Univ. of Iowa, Iowa City, IA, July 1992.

[13] Lien, F. S., and Leschziner, M. A., "Modelling the Flow in a Transition Duct with a Non-Orthogonal FV Procedure and Low-Re Turbulence-Transport Models," *Advances in Computational Methods in Fluid Dynamics*, edited by K. N. Ghia, U. Ghia, and D. Goldstein, ASME FED-Vol. 196, American Society of Mechanical Engineers, 1994, pp. 93–106.

[14] Gibson, M. M., and Launder, B. E., "Ground Effects on Pressure Fluctuations in the Atmospheric Boundary Layer," *Journal of Fluid Mechanics*, Vol. 86, 1978, pp. 491–511.

[15] Chen, H. C., and Patel, V. C., "Near-Wall Turbulence Models for Complex Flows Including Separation," *AIAA Journal*, Vol. 26, No. 6, 1988, pp. 641–648.

[16] Wilcox, D. C., "Reassessment of the Scale Determining Equation for Advanced Turbulence Models," *AIAA Journal*, Vol. 26, No. 11, 1988, pp. 1299–1310.

[17] Abid, R., Rumsey, C., and Gatski, T., "Prediction of Nonequilibrium Turbulent Flows with Explicit Algebraic Stress Models," *AIAA Journal*, Vol. 33, No. 11, 1995, pp. 2026–2031.

[18] Sofialidis, D., and Prinos, P., "Wall Suction Effects on the Structure of Fully Developed Turbulent Pipe Flow," *Journal of Fluids Engineering*, Vol. 118, No. 1, 1996, pp. 33–39.

[19] Lin, F., and Sotiropoulos, F., "Assessment of Artificial Dissipation Models for Three-Dimensional, Incompressible Flow Solutions," *Journal of Fluids Engineering*, Vol. 119, No. 2, 1997, pp. 331–340.

[20] Kim, W. J., "An Experimental and Computational Study of Longitudinal Vortices in Turbulent Boundary Layers," Ph.D. Thesis, Dept. of Mechanical Engineering, Univ. of Iowa, Iowa City, IA, Dec. 1991.

[21] Dauthieu, I., Laurence, D., and Richoux, S. (eds.), *Proceedings of 5th ERCOFTAC/IAHR Workshop on Refined Flow Modelling*, Electricité de France, Chatou (Paris), 1996.

[22] Menter, F. R., "Zonal Two Equation k-ω Turbulence Models for Aerodynamic Flows," *Proceedings of the AIAA 24th Fluid Dynamics Conference*, AIAA, Washington, DC, 1993, pp. 1–21.

[23] Patel, V. C., and Sotiropoulos, F., "Longitudinal Curvature Effects in Turbulent Boundary layers," *Progress in Aerospace Science*, Vol. 33, 1997, pp. 1–70.

[24] Luo, J., and Lakshminarayana, B., "Analysis of Streamline Curvature Effects on Wall-Bounded Turbulent Flows," *AIAA Journal*, Vol. 35, No. 8, 1997, pp. 1273–1279.

F. W. Chambers
Associate Editor